Reproducing and interpreting MHz Free Electron Laser X-ray Diffraction experiments by Finite Element Modeling

Nicolas Jaisle,[1, a)] David Cébron,[1, b)] Zuzana Konôpková,[2] Rachel J Husband,[3] Clemens Prescher,[4] Cornelius Strohm,[3] Hanns-Peter Liermann,[5] Orianna B Ball,[6] R Stewart McWilliams,[6] Valerio Cerantola,[2] Anand Dwivedi,[2] Karen Appel,[2] Khachiwan Buakor,[2] M. Nakatsutsumi,[2] Johannes Kaa,[7] Ulf Zastrau,[2] Carsten Baehtz,[2] Marzena Anna Baron,[8] J.D. McHardy,[9] Edward J. Pace,[9] Eric Edmund,[10] Lars Ehm,[11] Alexander F Goncharov,[10] Malcolm I McMahon,[9] Hyunchae Cynn,[12] Earl Francis O'Bannon,[12] Daniel T. Sneed,[12] B.T. Sturtevant,[13] S. C. Cooper,[13] Madison Anae,[11] Zhongyan Wu,[14] Yongjae Lee,[15] H-J. Hwang,[15] T.-H. Kim,[15] J.-H. Choi,[15] J.-M. Lee,[15] J-Y. Kim,[16] Z. Wu,[16] Hyunchae Cynn,[12] J. Biswas,[4] Sébastien Merkel,[8] Julien Chantel,[8] Egor Koemets,[17] Johannes Buchen,[17] Hauke Marquardt,[17] Vitali Prakapenka,[18] Stella Chariton,[18] Elena Shevchenko,[18] Guillaume Fiquet,[19] Angelika Rosa,[20] Mohamed Mezouar,[20] Gaston Garbarino,[20] and Guillaume Morard[1, c)]

[1)] *Univ. Grenoble Alpes, Univ. Savoie Mont Blanc, CNRS, IRD, Univ. Gustave Eiffel, ISTerre, 38000 Grenoble, France*

[2)] *European XFEL GmbH, Holzkoppel 4, Schenefeld, Germany*

[3)] *DESY Deutsches Elektronen-Synchrotron, Notkestr. 85, Hamburg, Germany*

[4)] *Institute of Earth and Environmental Sciences, Albert-Ludwigs University of Freiburg*

[5)] *Photon Science, DESY Deutsches Elektronen-Synchrotron, Notkestrasse 85, Hamburg, Germany*

[6)] *School of Physics and Astronomy, University of Edinburgh, UK*

[7)] *Tech. Univ. Dortmund Fakultät Physik/DELTA, Maria-Goeppert-Mayer-Straße 2, 44227 Dortmund, Germany*

[8)] *Univ. Lille, CNRS, INRAE, Centrale Lille, UMR 8207 - UMET, F-59000 Lille, France*

[9)] *School of Physics and Astronomy, University of Edinburgh, Edinburgh, UK*

[10)] *Earth and Planets Laboratory, Carnegie Institution for Science, Washington, DC, USA*

[11)] *Dpt. of Geosciences, Stony Brook University, 255 Earth and Space Sciences Building, Stony Brook, New York, USA*

[12)] *Lawrence Livermore National Laboratory, USA*

[13)] *Los Alamos National Laboratory, USA*

[14)] *Dpt. of Physics, Hanyang University, 17 Haengdang dong, Seoul, South Korea*

[15)] *Yonsei University, Department of Earth System Sciences, Republic of Korea*

[16)] *Hanyang University, Republic of Korea*

[17)] *Dpt. of Earth Sciences, University of Oxford, United Kingdom*

[18)] *University of Chicago, CNM, ANL USA*

[19)] *Institut Minéralogie, de Physique des Matériaux et de Cosmochimie, Sorbonne Univ., 4 Place Jussieu, Paris, France*

[20)] *European Synchrotron Radiation Facility, Grenoble, France*

(Dated: 21 February 2023)

A new diamond anvil cell experimental approach has been implemented at the European X-ray free electron laser, combining pulsed laser heating with MHz X-ray diffraction (XRD). Here we use this setup to determine partial or full melting under extreme conditions, based on the determination of time resolved crystallization sequences. The focus is on a Fe-Si-O ternary system, relevant for planetary cores. This time-resolved diagnostic is complemented by a finite element model, reproducing the temporal temperature profiles measured experimentally using streaked optical pyrometry. Benchmarked with previous studies using finite element modeling solutions, our model includes pressure and temperature dependencies of material properties such as thermal conductivity, thermal equation of state, heat capacity, melting temperature and latent heat. In addition, we implemented heat-induced thermal stress and its feedback effect on material parameter variations. Near infrared laser intensities are determined by seeking minimal deviation between measured and modeled temperatures. Modeling enhances streak optical pyrometry data by providing inner temperature distribution and extending temperature determination below detection limit (ranging between $1500 - 3000$ K). Temperatures obtained by the model are in excellent agreement with the reported crystallization temperature of Fe-Si alloys around 60 GPa. In addition, the presented approach could be used to infer the liquidus temperature by the appearance of SiO_2 diffraction spots. Our model reproduces high-pressure, high-temperature experimental conditions, allowing prediction of temperature, pressure and volume conditions, and then determine liquidus temperature before strong chemical migration occurs. This kind of synergy of novel time-resolved experiments and finite-element modeling pushes further the interpretation capabilities in diamond anvil cell experiments.

[a)] nicolas.jaisle@univ-grenoble-alpes.fr

[b)] david.cebron@univ-grenoble-alpes.fr

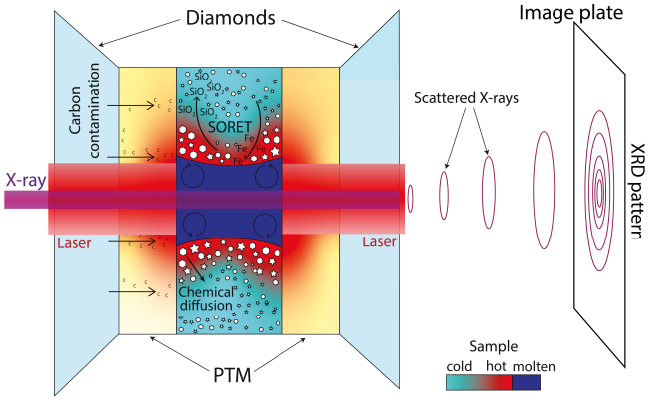

FIG. 1. Schematic representation of potential biases in laser heated diamond anvil cell experiments (not to scale). Temperature gradients inherent to laser heating might lead to i) Carbon diffusion from the diamond anvil, leading to sample contamination, ii) convection inside the molten sample leading to enhanced chemical interaction at the solid-liquid interface, iii) Soret diffusion[10,11] leading to transfer of lighter elements towards hot zone and heavier elements towards cold zone as observed on Fe-Si-O alloy[12]. iv) chemical diffusion, possibly leading to compositional gradient. The mineralogical assemblage probed by XRD and used to infer phase melting might therefore not correspond to the pristine sample compositions.

I. INTRODUCTION

Determination of partial melting properties in geomaterials is crucial to understand planetary evolution, from the early differentiation during the magma ocean stage to the core crystallization and its impact on magnetic field generation[1,2]. Laser-heated diamond anvil cell (LH-DAC) experiments combined with XRD is a commonly used method to probe partial melting under high pressure and high temperature conditions. Yet, the measurements achieved at such high pressures and temperatures are sometimes unable to accurately determine the liquidus temperature, due to chemical migration induced by temperature gradients. Therefore, results from melting experiments using LH-DAC can exhibit large discrepancies between each other[3–5]. Different chemical migration processes were suggested to explain those discrepancies including carbon contamination[6] and pressure overestimation[3].

During LH-DAC experiments, only surface temperature is calculated from emission spectra but without information about inner temperature distribution. Recent developments in multispectral radiometry allow to measure surface temperature distribution[7], however modeling remains necessary, especially for highly absorbing metallic samples where laser heating generates huge axial temperature gradients[5,8,9].

Indeed one of the most problematic issues related to temperature gradients is the consequent chemical migration inside the sample (Fig. 1). Chemical migration was observed in various studies in the solid state[11,13] or related to partial melting[12,14]. Different phenomena were suggested to explain this chemical migration in the presence of temperature gradients. Among those, one of the most discussed is the so-called Soret effect[10,11]. In addition, the surface tension[15] as well as the convection upon melting[16] could cause chemical migration inside the partially molten sample. All these effects induce a chemical gradient between the hot and cold part of the sample, with the probed area then having a different composition from the initial bulk one. In order to minimize this chemical migration, a new experimental approach has been developed, combining time-resolved X-ray diffraction and pulse laser heating. The MHz pulse train structure of the European X-ray Free Electron Laser (EuXFEL) is particularly suited to study partial melting at µs time scale under extreme conditions. This µs heating is assumed to lead to few or no chemical migration while EuXFEL provides pulse intensities high enough to obtain good diffraction patterns[17]. Experiments performed at EUXFEL at 2.27 MHz X-ray pulse frequency (one pulse every 440 ns) and acquired with an Adaptive Gain Integrating Pixel Detector (AGIPD) 500k, capable of acquiring separately each pulse. Upon each pulse train, streak optical pyrometry (SOP) was performed in order to obtain surface temperature data along with the XRD data. To be more finely constrained, temperature analysis and XRD data are complemented by numerical modelling, which is done with the Finite Element Method (FEM) using the COMSOL commercial software. FEM can give knowledge about the temperature distribution inside the sample, the gradients generated during the pulsed heating phase and the cooling phase as well as evaluate the thermal stress. Differences between simple parametric temperature estimates in the pressure medium[18] and FEM model results[19] highlight their importance for LH-DAC experiments. The presented experiment is focused on probing the Fe-Si-O ternary phase diagram, Si and O being two possible major light elements in the liquid outer core[20]. Fe-Si-O moreover represents an archetypal example of chemical migration in LH-DAC[12]. Using a intense short (250 ns) laser pulse (shape provided in Appendix A) at 1060 nm to heat our sample, we investigated the crystallization sequence using XRD, this alloy decomposing into $FeSi$ and SiO_2 upon cooling with almost no chemical migration. Therefore, the liquidus temperature could be measured under high pressure which is normally complex under standard LH conditions.

In this paper, an overview of the experimental LH-DAC setup is first provided in section II, together with the methods used for sample heating, XRD analysis achieved at the EUXFEL, and *post-mortem* analysis. Then, the section III describes our FEM model, reproducing the experimental conditions by using laboratory values and detailed material parameters taking into account heat transfer and thermal pressure. Results and model are presented in section IV output after adjustment with the data, and how model can enhance available temperature data and XRD interpretation and discussion. Section V concludes with some suggestion of future model improvements.

c)guillaume.morard@univ-grenoble-alpes.fr

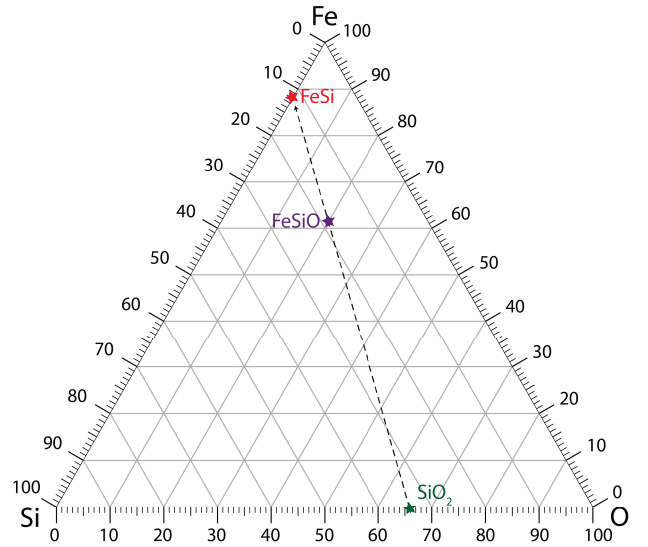

	Atomic %	Wt %
FeSiO	61.1% Fe-18.9% Si-20% O	80.2% Fe-12.35% Si-7.45% O
SiO_2	66.7% O - 33.3% Si	46.67% Si-53.33% O
FeSi	12.5% Si-87.5% Fe	7% Si-93% Fe

FIG. 2. Demixing line of the ternary Fe-Si-O system. The blue point highlights the initial FeSiO alloy composition used during our experiment. The dashed arrow represents the chemical pathway followed by the sample as it cools down. This allows inferring the formation of SiO_2 (lower right green star) out of the initial alloy (purple star) until only pure FeSi remains (upper left red star). The final Fe-Si ratio in the formed Fe-Si alloy (around 8 wt% Si) is thus controlled by the initial composition.

II. METHODS

Experiments were performed at the High energy density (HED) instrument[21] at the EuXFEL using the dedicated DAC set-up in interaction chamber 2 (IC2)[17,22]. For our experiment, we used symmetric cells[23] equipped with Boehler-Almax conical supports and diamonds[24] with a large aperture of 70° on the opposite side of X-ray arrival direction (downstream), suited to get a wide diffraction angular range and a standard diamond on X-ray arrival side (upstream). The sample chamber drilled in a Re gasket pre-indented to 50 µm was loaded with an assembly of two KCl disks (diameter 120 µm and thickness of 20 µm) surrounding an Fe-Si-O alloy sample (Fig. 2) with a diameter of approximately 60 µm and 8 µm thickness. This alloy consists of 80.2 wt% Fe, 12.35 wt% Si and 7.45 wt% O (by microprobe verified composition) and was synthesized by plasma vapor deposition (PVD) (Dephis company)[12].

KCl was chosen as pressure transmitting medium (PTM) because it is not considered to react with iron[3,26] in addition to its good thermal insulation. In addition, the KCl can be used as an internal diffraction standard by monitoring the XRD peak shift (and thus lattice volume change) related to pressure by its equation of state (EoS)[27]. After loading, the entire cell is kept inside a vacuum oven kept at 120°C in order to ensure dehydration and thus absence of water inside the sample chamber. The pressure on the sample was increased by tightening the screws and measured using the KCl.

The experiment was performed inside interaction chamber 2 (IC2) using the DAC platform. High sample temperatures were generated using double sided, on-axis, pulsed laser heating (SPI G4 laser with lambda = 1064 nm) with a 250 ns pulse length. The temporal laser profile is shown in appendix A.

The laser is coming from a single source which, injected in the optical path by a dichroïc mirror, is then split into two beams along the optical path and brought to the sample's surface by a series of lenses. Incoming laser intensity on the sample's surface can be controlled by the polarizing beam splitting cubes (polarizors) and rotating waveplates in each laser beampath, going upstream and downstream of the DAC. The gaussian shaped laser focal spot size was $12-13$ µm full width at half maximum (FWHM) (measured with the Thorlabs optical beam profiler). Based on the prediction of the alloy's corresponding ternary phase diagram (Fig. 2), the formation of SiO_2 and FeSi are expected upon sufficiently high laser heating (typically above SiO_2 melting temperature aroung 4000-5000 K). To achieve this, we use a single laser pulse in order to limit heating duration below the microsecond and keep the composition as close as possible to the initial one in order to follow the expected chemical pathway (i.e. to perform the experiment faster than any chemical migration might happen).

SOP data was collected using a Hamamatsu streak camera with a S-20 photocathode coupled to a Princeton Instrument spectrometer to acquire the optical surface emission on the downstream side. The camera's sweep window was set to 5 µs. Calibration was done with a tungsten incandescence standard lamp used as a thermal source with a known temperature of 2900 K.

Temperature measurement using a streak camera is essential for the short timing of the present experiment (5 µs), however the drawback is a reduced sensitivity. Only temperature measurements above 4000 K were reliable, requiring an extrapolation for a longer time, and a lower temperature.

The experiment was performed using a photon energy of 18 keV (λ = 0.6968 Å) producing high-brilliance pulse trains (about 10^{10} photons per pulse)[22]. In agreement with the expected sample cooling duration after a laser pulse, data were collected using a pulse train with up to 40 pulses with a 440 ns separation (2.27 MHz repetition rate) that totals 17.16 µs. Due to self-amplified spontaneous emission's (SASE) nature at XFELs, the relative intensities of the pulses inside a train can fluctuate and were measured for each train[22]. The X-ray beam was focused using a series of compound refractive lenses (CRLs) to a diameter below 10 µm, smaller than the laser spot size to ensure probing a homogeneous temperature distribution. Attenuators are used to limit X-ray intensity with can be high enough to induce heating as demonstrated by previous experiments[28,29]. However, the experiments presented in this study were performed with the aim of minimizing substantial X-ray heating. To ensure this experimentally, we performed preliminary runs in order to assess the amount

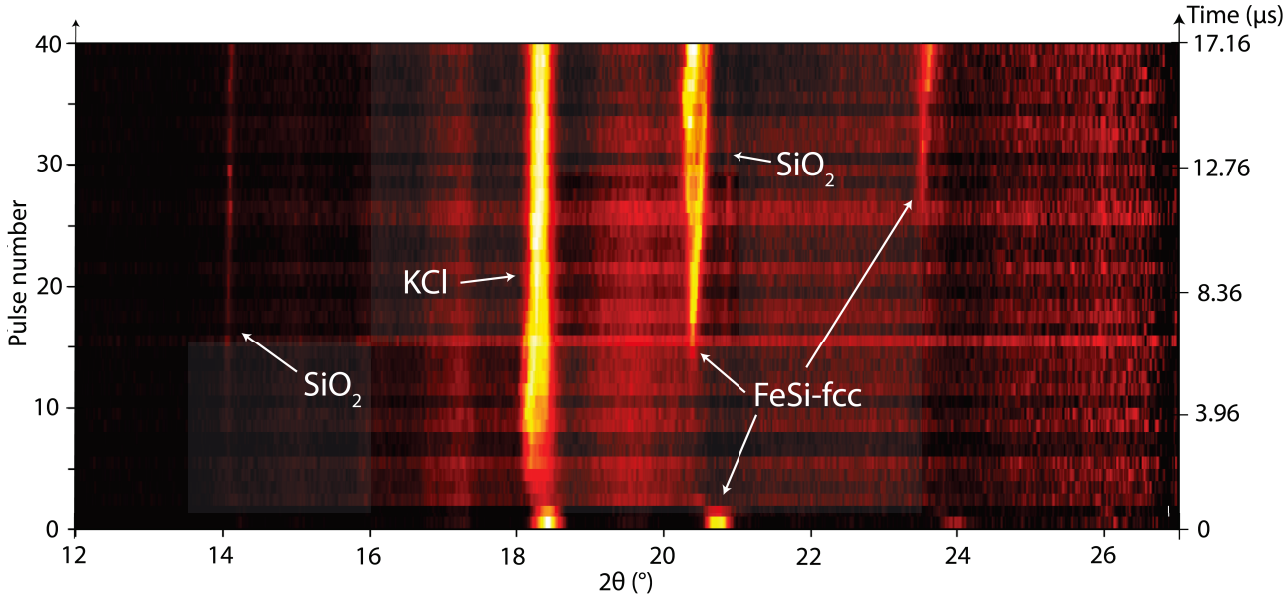

FIG. 3. Batch view of pulse train diffraction spectra series[25]. The pulse frequency was 2.27 MHz (time range span of 17.16 µs for 40 pulses). The moments where phases are first observed (spawn times) can be constrained by seeking the line apparition and checking for spots on the image plate. Observable phases are highlighted and designated. The KCl peak partly fades over the first pulses where the maximum fiber laser intensity is delivered to the sample, meaning that it is likely almost entirely molten inside the X-ray sampling zone. The first sample phase to crystallize upon cooling is SiO_2. It is observed for the first time on the diffraction spectra at 2.2 µs (time zero corresponding to the first X-ray pulse). The FeSi-fcc peaks entirely disappear within the first 3 pulses before re-appearing at 5.72 µs for the left peak. Note that the second and fainter higher angle peaks of FeSi-fcc and SiO_2 appear later in time, likely due to signal degradation at higher angles and crystal tininess.

of X-ray transmission needed to generate detectable heating. Heating was quantified by the sample's main diffraction peak shift within a pulse train. Once the absence of X-ray heating was ensured, the sample was moved to an unheated position. On this fresh spot, a YAG laser pulse was applied simultaneously to the attenuated X-ray pulse train. The absence of X-ray heating in the data was checked as well by varying X-ray intensity model input and is explained more in detail in the supplementary material. Spatial alignment between laser and X-ray was ensured before the shot. The sample was laser heated in different locations (see diffraction map in supplementary material). The adjustable delay between the X-ray and laser pulse was set to synchronize heating and probing; starting the laser and X-ray pulse train simultaneously. The delay between pump and probe was set so that the first acquired X-ray pulse furnishes a diffraction spectra of the bulk sample at ambient temperature. Note that the SOP acquisition is shifted compared to this starting moment and its acquisition starts 0.521 µs earlier than the laser pulse and 0.22 µs earlier than the first X-ray. Additionally to the laser heating, one has to account for X-ray heating enabled by the short but intense X-ray pulses heating on top (up to 10000 K for Fe sample[28,29]). To prevent that, the X-ray pulse intensity was lowered by using attenuators in the beam path to obtain a good balance between sufficient XRD signal and no or weak X-ray heating. Once the attenuation was well adjusted, the laser heating pulse intensity was raised stepwise, up to the value where complete melting and crystallization sequence was observed in the XRD data at different sample positions. For this study we focused on one run where the heating produced full melting.

Pulse-resolved XRD data were collected with an AGIPD[30,31] at the intra-train repetition rate of the XFEL pulse train (2.2 MHz). AGIPD was positioned outside of the vacuum chamber. The sample-to-detector distance (422.3 mm), detector tilt and rotation were calibrated using CeO_2 diffraction standard in the DIOPTAS software[25]. Diffraction images were radially integrated using DIOPTAS to produce 1D diffraction profiles for the image sequence of the complete train plotted against 2Θ (see Fig.3).

For complementary *ex-situ* observations and measurements under scanning electron microscopy (SEM), the sample was cut using a focused ion beam (FIB) at the EuXFEL (Appendix B). Relative composition analysis of heated vs non-heated sample was achieved with energy-dispersive X-ray spectroscopy (EDS).

III. FINITE ELEMENT MODEL

Finite element modeling gives access to certain measurements which are not available in DAC experiments, and allow temporal interpolation of the experimental data[16,28,32]. Here, the temperature field is calculated, extending on many aspects the few previous COMSOL finite element models[28]. In particular, and by contrast with previously published models,

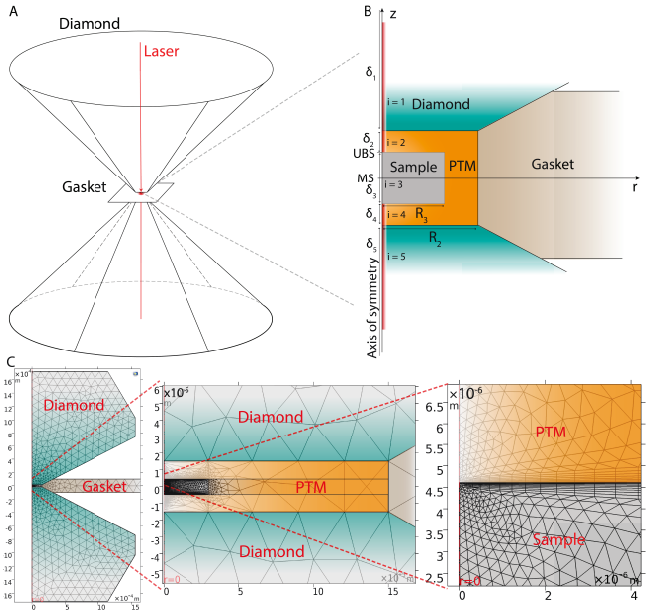

FIG. 4. A) Schematic of the DAC setup used in our numerical model. B) Zoom on our FEM 2D-axisymmetric geometry (not to scale), z-axis being the axis of symmetry in the cylindrical coordinates (r, z). Each domain has its specific properties (density, thermal conductivity, heat capacity...). UBS stands for upper border of the sample and MS for middle of the sample. C) Actual mesh example used in the simulation. Mesh is more finely constrained towards important boundaries (PTM/sample)

the present model (i) includes the various EoS of the materials involved in our experiments, as well as their influence on the pressure induced geometry deformations, (ii) includes thermal and pressure dependencies of the parameters, (iii) combines laser and X-ray thermal heating, and (iv) takes into account the feedback of the thermal stress[33,34]. As the temperatures reached in this work are high enough to melt materials in our experiments, possible liquid flows have been tested on the model, following previous works[16]. However regarding neglectable flow effects on the heat transfer[16], the liquid domains were from there on assumed to be at rest in present computations.

Using the cylindrical coordinates (r, z), the geometry of our axisymmetric DAC numerical model is sketched in the figure 4 and the geometrical parameters are given in Table I. Note that the pressure P_{ref} imposed on the DAC leads to important initial geometry deformations, which have to be taken into account. Having first calculated the complete elastic deformations of the geometry, our preliminary tests show that the various mechanical contacts between the different media raise several numerical issues (e.g. domains separation since the media are not glued). As a first step, the model used here only accounts for the relevant leading order effects by simply changing the various media thickness in the model using the material EoS of each medium (our model is detailed in Appendix C).

Our extended numerical DAC model aims at providing the temperature distribution at the reference pressure P_{ref}, in-

TABLE I. Geometric parameters of the COMSOL model. Parameters with single value are fixed. Parameters with single value are fixed. Parameters with two values change during computations. In such case first values are initial ones measured at ambient conditions. Second values are those used in the model once pressure was applied ($P_{ref} = 61.9$ GPa throughout this work) using EoS. Those values remain constant over simulation. Dimensions are listed in numerical order from upstream to downstream (the index i corresponds to the different media ($i = 1$: upper diamond, $i = 2$: upper PTM...))

Medium	radius R_i [µm]	thickness δ_i [µm]
Diamond (i=1, 5)	2000	160
PTM (i=2, 4)	40	$9 \mid 4.983$[a]
Sample (i=3)	40	$5.5 \mid 4.345$[a]
Gasket	120	$\delta_3 + 2\delta_2$

[a] $P_{ref} = 0 \mid P_{ref} = 61.9$ GPa

cluding thermal stress effects (pressure induced variations of the material parameters due to thermal expansion and boundary constraints). By contrast with previous models[16,28], this requires integrating the elastic equations together with the heat transfer equation. Considering quasi-static infinitely small displacements (negligible inertia), the stress tensor $\boldsymbol{\sigma}$ and the temperature T are governed by

$$\rho C_P \frac{\partial T}{\partial t} + \boldsymbol{\nabla} \cdot \boldsymbol{q} = Q, \tag{1}$$

$$\boldsymbol{\nabla} \cdot \boldsymbol{\sigma} = 0, \tag{2}$$

where the heat flux vector $\boldsymbol{q} = -k_{th} \nabla T$ is given by Fourier's law, with the volume heat source Q (e.g. due to radiation absorption, as detailed in section C 2), and where all the physical parameters (ρ, C_P, k_{th}) of equation (1) depend a priori on space via their pressure and temperature dependencies (ρ being the material density, C_P the heat capacity at constant pressure, and k_{th} the thermal conductivity). However, these dependencies are generally not known and the material parameters have thus been taken as constant except for the KCl PTM density, and for the parameters (ρ, C_P, k_{th}) of the sample (see Table II). The boundary conditions and initial state used in our model to integrate equations (1)-(2) are provided in the appendix C 3.

Due to sparse literature on FeSiO material properties and its high Fe content, the sample parameters have been assumed to be similar to pure Fe (i.e. sample has properties of Iron in the model). As simulations are generally performed at high pressures ($50 - 100$ GPa), only the high pressure, high temperature phases (ϵ-iron[35] (hcp), γ-iron[36] (fcc) and liquid Fe[37]) EoS were considered, where liquid Fe EoS employs a recently developed method to characterize the structure of liquids under high pressure as described in Morard et al. 2013[38]. Similarly for KCl, only the EoS of the B2-KCl[27] (high pressure phase) was considered. To obtain the density from EoS at a given temperature and pressure (T, P), we have used the EoS to calculate ρ on a large (T, P) range and the value used by our numerical model at each time step is then obtained by a 2D interpolation. When the needed values were

out of the EoS validity range, as e.g. liquid Fe at very high temperatures, the density was assumed constant and equal to the closest value inside the validity range. The validity range (above ~ 15000 K) has only been exceeded over a very short time, at the peak temperature reached at the maximum laser pulse intensity.

The pressure and temperature dependencies of k_{th} for the sample are obtained from the literature (Table II). This value predominantly controls the temperature field evolution (i.e. axial, radial), as well as in terms of temperature decay rate. The C_P dependencies are more difficult to obtain, for instance for the hcp phase of iron. Here, C_P of the fcc phase of iron is obtained by combining thermodynamic relations (Appendix C); these expressions being also used (beyond their validity regime) to provide C_P estimates for the hcp phase of iron. Regarding C_P, the value effectively used in our numerical model is also affected by the latent heat of possible phase changes. The high temperatures reached in our experiments can indeed melt the materials, and phase change effects have thus to be taken into account. To do so, the apparent heat capacity method (AHCM) is used (Appendix C), and the values of C_P and k_{th} are modified when phase changes occur (our model only considers AHCM for liquid-solid phase changes).

To integrate equation (2), a material rheology has to be chosen. A recent study highlights that non-isotropic deformation have an impact on pressure medium and sample final thickness, and therefore on later conductivity measurements in LH-DAC[45]. Reproducing this non-isotropic deformation yet demands more evolved models and we chose not to include it in this model. Here, the materials are all assumed to follow the usual Hooke's law for isotropic materials. Noting the elastic displacement $\boldsymbol{u}$, this law relates $\boldsymbol{\sigma}$ to the (infinitesimal) strain tensor $\boldsymbol{\epsilon} = [\nabla \boldsymbol{u} + (\nabla \boldsymbol{u})^\top]/2$ by

$$\boldsymbol{\sigma} = K\left[\mathrm{Tr}(\boldsymbol{\epsilon}) - \alpha_V (T - T_{ref})\right]\boldsymbol{I} + 2G\,\mathrm{dev}(\boldsymbol{\epsilon}), \qquad (3)$$

with the bulk modulus K, the shear modulus G equals zero in liquid domains, and the deviatoric strain tensor, also called shear tensor, defined by $\mathrm{dev}(\boldsymbol{\epsilon}) = \boldsymbol{\epsilon} - \mathrm{Tr}(\boldsymbol{\epsilon})\boldsymbol{I}/3$. Equations (1) and (2) are thus fully coupled both ways: thermal stresses are generated by the T variations in the equation (2) while the associated thermal pressure P_{th} modifies the physical parameters (ρ, C_P, k_{th}) in equation (1), e.g. for the sample in this experiment.

The volumetric coefficient of thermal α_V expansion[33] is related to the (linear) secant coefficient of thermal expansion α_L through $\alpha_V = 3\alpha_L$ since the thermal stress $\boldsymbol{\epsilon}_{th}$ is $\boldsymbol{\epsilon}_{th} = \alpha_L(T - T_{ref})\boldsymbol{I}$, where T_{ref} is the reference temperature at which there are no thermal strains. Contrary to equation (1), all the physical parameters (K, G, α_L) of equation (2) are assumed to be constant in this work and are provided in table II (K and α_L can be deduced from the EoS, adding a coupling between equations 1 and 2). The total pressure $P_{ref} + P_{th}$ is then obtained from the thermal pressure $P_{th} = -\mathrm{Tr}(\boldsymbol{\sigma})/3$, which is *a priori* non-uniform in the domain.

Because of its multi-physics nature, our axisymmetric numerical model is developed using the finite element commercial software COMSOL, which is well suited for such modelling. It is important to notice that numerical difficulties are raised by the large disparity of time and space scales involved in our DAC numerical model. To ensure accurate integration in space and time of equations (1)-(2), special care has thus been taken concerning the mesh and the time-stepping (Appendix C).

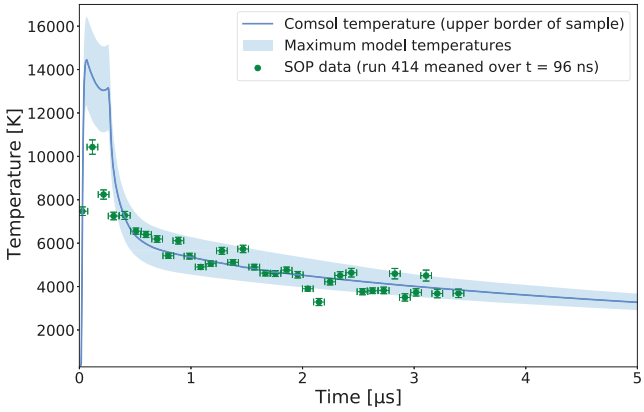

FIG. 5. Temperature vs. time for run 414 on FeSiO at $P_{ref} = 61.9$ GPa. Green dots are measured SOP data and solid line is COMSOL best fit. Solid line shows temperature modelled at the sample's surface within the error bar corresponding to the two next best models above and below in terms of intensity. Comparison between SOP and model is done with model averages over 96 ns time step. Error bars for SOP data are from the SOP analysis output.

IV. RESULTS AND DISCUSSION

The present study combines FEM modeling with newly designed MHz XRD in pulsed LH-DAC experiments, which constitutes an innovative scientific approach to study partial melting under high pressure. After the description of the experimental and numerical methodology, the application on partial melting in the ternary Fe-Si-O system will be hereby described with Fe-Si alloy and SiO_2 crystallization points extracted from model and XRD measurements combination.

An example of SOP raw data and Planck fitting used to obtain temperature data can be found in the supplementary material. The peak SOP temperature is poorly resolved due to its short duration (less signal) and possible signal saturation at very high temperatures, whereas the temperature decay over several microseconds is well constrained.

A FEM model including laser heating only is adjusted on the SOP data by finding the proper incoming intensity which minimizes the difference between model temperature evolution at upper border of the sample (UBS) (Fig. 4) and SOP. Results for one run are shown in Fig. 6 and highlights (Fig.6 A.) that the optimal laser energy has the same order of magnitude than the energy measured experimentally at the output (around 1 mJ before being split in two parts). Differences could be explained by the energy loss along the optical path.

TABLE II. List of material properties used for our simulation. All parameters mentioned by "var." are those varying with the model temperature and pressure outputs. References for those variations are given in the footnotes of this table. When the same value is used for different phases, those are mentioned in parenthesis. If only one value is given this means the same was used for all phases. X-ray absorption coefficients[28] are given for 25 keV and laser absorption coefficients are given for a 1 μm wavelength. When only one value specified, this means that the same value is used for every phase.

	Fe (hcp/fcc/liq)	KCl (sol/liq)	Diamond	Re
μ_{Laser} $[\text{m}^{-1}]$[a]	∞	7×10^{-4}[b]	0.3[c]	0
$\mu_{\text{X-ray}}[\text{m}^{-1}]$ (18 KeV)	26316[d]	2513[d]	158[d]	0
C_{P} $[\text{J.(kg.K)}^{-1}]$	var.[e](hcp,fcc)/900[41]	690.72[f]	630[g]	140[28]
$k_{th}[\text{W.(m.K)}^{-1}]$	var.[42]	6.53[f]/0.344[43]	1500[g]	48[g]
$\rho[\text{kg.m}^{-3}]$	var.[35]/var.[36]/var.[37]	var.[27]/var.[44]	3520[28]	21020[28]
α_L $[\text{K}^{-1}]$	12×10^{-6}	36.5×10^{-6}	0.8×10^{-6}	6×10^{-6}
G [GPa]	78[h](hcp/fcc)/0	6.24[f]/0	440[i]	182[j]
K [GPa]	160[k]	17.36[f]	530[i]	312[j]

[a] See supplementary material
[b] Hass et al. 1976[39]
[c] Values for IIa diamonds[40]
[d] https://henke.lbl.gov/optical_constants/atten2.html
[e] Relationship detailed in Appendix C
[f] https://www.crystran.co.uk/optical-materials/potassium-chloride-kcl
[g] Meza-Galvez 2020[28] (at 25 keV)
[h] AZO materials
[i] https://www.azom.com/properties.aspx?ArticleID=262
[j] https://www.azom.com/properties.aspx?ArticleID=1491
[k] https://www.azom.com/properties.aspx?ArticleID=619

Fig. 6 plots the mean error at different laser intensities between SOP temperature data and FEM model on one heating spot for the FeSiO alloy. Model with lowest mean error is kept and used to plot the corresponding COMSOL temperature curves as a function of time (Fig. 6). A good agreement between the SOP temperature data and the COMSOL extracted data can be found after the minimization. Using this model we can extrapolate the lowest temperature inside the 5 μm radius cylinder around the axis of symmetry in the sample.

This minimum temperature curve can be compared with the FeSi-fcc phase spawn point (Fig. 6). The time of crystallization is obtained by the time apparition of the FeSi-fcc on the diffraction spectra (Fig. 3). As a first approximation the pressure is considered to be the initial one measured within the KCl volume (62 [GPa] for the example in Fig. 6). An excellent agreement can be observed between extrapolated SOP data and expected crystallization temperature[46] ($2000 - 3000$ K around 60 GPa).

The pressure could be accurately determined for each time step during the sample cooling. Taking the KCl volume at the spawn moments and the extrapolated temperatures of the FEM models, we calculated the estimated mean temperature in the PTM with a method described by Campbell et al. 2009[18]. Even if the peak of KCl broadens due to the temperature gradient, the mean peak position was picked assuming this to correspond to the mean PTM lattice volume. Finally the pressure can be calculated through the EoS[27]. Another method to estimate the mean sample thermal pressure directly obtained from the FEM model, as described in the section dedicated to thermal stress.

In the ternary Fe-Si-O phase diagram, the crystallization of the Fe-Si alloy is expected not to incorporate any oxygen[12] and therefore fall on the Fe-Si binary system (Fig. 2). Following the demixing line, the Fe-Si alloy crystallizing contains 7wt%Si.

Crystallization time for Fe-Si alloys are bracketed between fully molten and first solid crystal appearance. Pressure and temperature were evaluated by combining model output temperature (minimum temperature within sample inside a r=5μm) and (i) pressure obtained with P(V,T) EoS[27] using calculated mean temperature in KCl[18]) and volume obtained by XRD) or (ii) mean thermal pressure in sample (over r=5μm) from model output. Melting points obtained by the two methods lie within the error bars (Fig. 7) compared with two close in composition Fe-Si alloy melting curves (Fe-7wt%Si[46] and Fe-9wt%Si[48]). The absence of thermal stress feedback in the PTM temperature in the first case explains observed pressure differences with the second case, where thermal pressure is modeled inside the sample.

Both pressure and temperature estimations are then compared with the Fe-Si alloys melting curves (Fig. 7) taken from existing literature[46,48]. Despite the different thermal pressure depending on the assumption, we can observe an overall agreement between our measurements and the existing literature.

Recrystallization of SiO_2 from the melt is not ubiquitous over the different runs on the FeSiO samples. As SiO_2 is recrystallizing in few small crystallites moving within the molten sample without preferred orientation. This generates an inconstant diffraction signal which does not always reach the XRD detector. In addition the scattering intensity of SiO_2 is relatively weaker than those of Fe-Si alloys. Finally, the downstream mirror is slightly shadowing the low

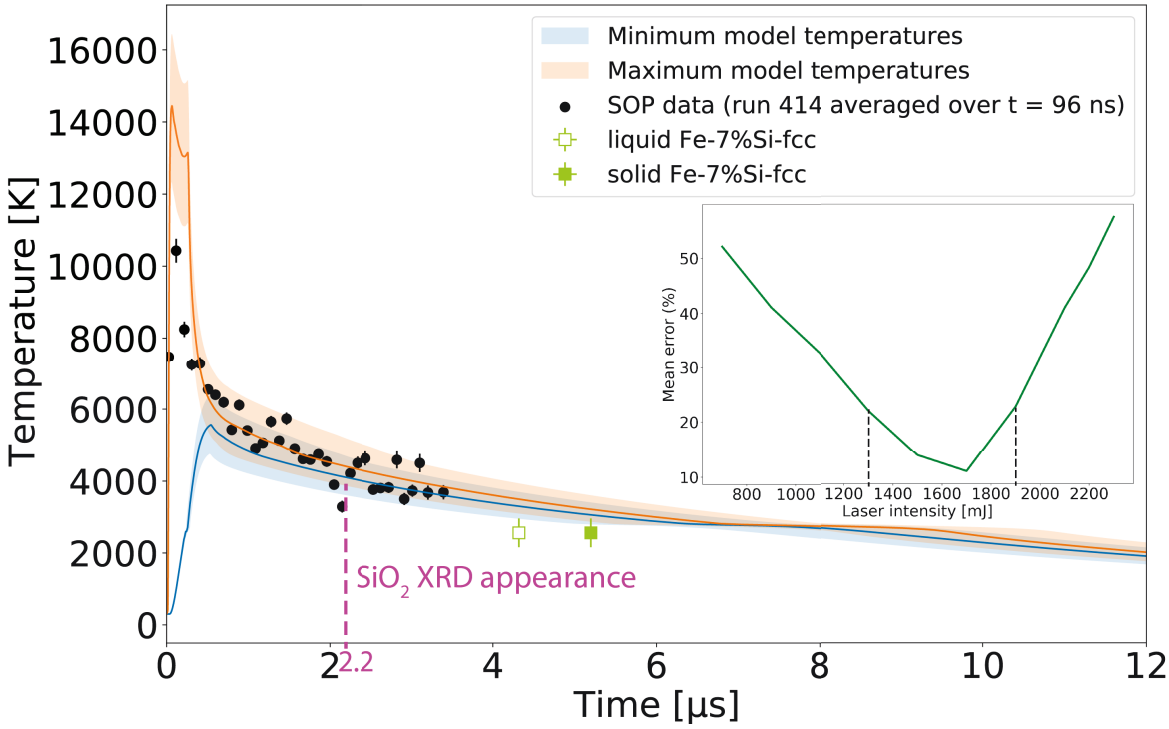

FIG. 6. Example of model adjustment to experimental data for a single run (one 40 X-ray pulse train). Temperatures vs time obtained from FEM model for the minimal mean error for a given run (#414), the continuous orange line being the UBS temperature on the axis of symmetry. Green and orange dots are respectively SOP and model values averaged over 96 ns. Dashed blue curve plots minimum temperature in sample inside the X-ray sampled zone (X-ray radius assumed constant for each run : r = 5 µm). Red star highlights FeSi apparition moment observed by XRD 183 K below melting temperature of Fe-7 %Si-fcc phase[46] where phase transition is expected[47].Vertical dashed pink line indicates the time where SiO_2 is unambiguously observed by XRD (2.2 µs). Inset: Mean error between FEM UBS and SOP temperature for several laser intensities (reproducing waveplate rotation angle modifications) for run 414 on an FeSiO sample at 61.9 GPa. In that case the rotation angle was 15° on both sides (upstream and downstream). The relationship between measured intensity and wave-plate rotation angle can be found in supplementary material. Vertical black dotted lines bracket best models obtained within error of 20% chosen as error bar.

diffraction angles on the X-ray detector. For all those reasons, it is complex to identify the first crystallization of SiO_2. We assume a first appearance at 2.2 µs, which corresponds to a lower temperature limit of 4400 K. Comparing this temperature with the crystallization of pure SiO_2 (5200 K[49]) we can potentially extract the liquidus temperature of FeSiO ternary system. However, due to the difficulty of finding the precise spawn time, this is an upper limit and SiO_2 might be present before as suggested by Fig. 6.

A main goal of the experiments was to limit chemical migration during laser heating. As proof of concept, we analyzed the chemical composition of several heating spots after heating. Fig. 8 presents a typical heating spot obtained by a single laser pulse impact. The table in Fig. 8 compares the mean relative chemical composition in weight percent between the pristine sample and heated zone spots.

These relative concentrations demonstrate that the use of a short-time scale heating pulse allows toreduce chemical migration compared to longer timescale heating where chemical migration is observed on the FeSiO alloy[12] with SiO_2 accumulating at the heating spot external boundaries.

Furthermore, as previously discussed, chemical migration is related to temperature gradients, which can be determined with our model (Fig.9). Indeed figure 9 highlights differences between UBS, middle of the sample (MS), minimum and maximum temperatures inside the 5 µm radius cylindrical zone sampled by the X-rays as a function of time. During the first 250 ns, there are temperature gradients of the order of 10^4 K in the probed volume. A first temperature homogenization occurs after 1 µs with around 900 K between minimum and maximum temperature within the X-ray sampled zone (Fig. 9 B.). Later, around 7 µs, this temperature gradient is reduced to 70 K, confirming the local temperature homogeneity inside the X-ray sampled zone at that time. Migration time scales observed in continuous laser heating thus occur at longer time scales than the µs.

V. CONCLUSION

This study validates a new approach where crystallization sequences upon cooling from a liquid state with no (or very limited) chemical migration due to heating are reproduced. Diffraction data collected during several heating cycles (Fig. 3) combined with chemical analysis (Fig. 8) confirmed the reduced amount of chemical migration induced by short laser

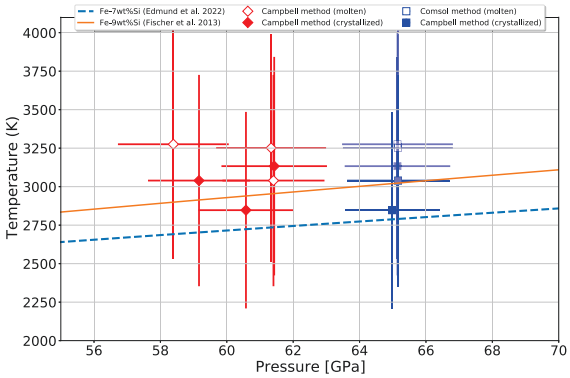

FIG. 7. FeSi-fcc melting points at pressure inferred from two methods: 1) Red diamonds represent the melting points at pressures calculated with the KCl EoS[27] by using the FEM model PTM/Sample on-axis temperature output to calculate the mean PTM temperature with the method described by Campbell et al. 2009[18]. 2) Blue squares for the mean pressure output from our model (including thermal stress). In both cases, the EoS input lattice volume is the one obtained from the KCl mean peak position. Dotted blue line is melting curve for Fe with 7 wt%Si[46] and continuous line melting curve for Fe with 9 wt%Si[48]

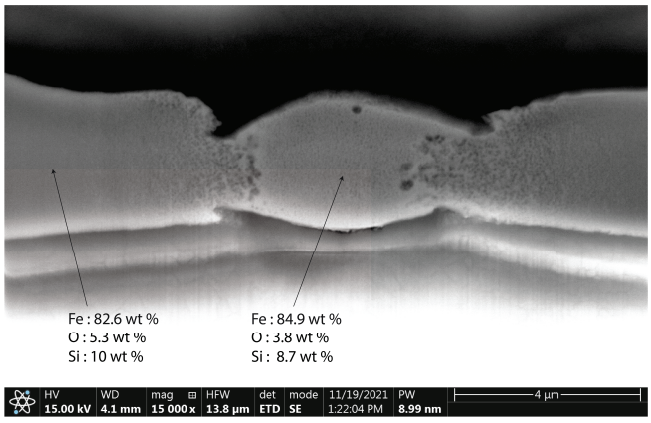

FIG. 8. SEM cross section of an FeSiO alloy after sample heating at 30 GPa. The heated region (centre) appears homogeneous, with possible grain growth and/or chemical migration at the heating spot edges. The pressure medium is KCl. Major element distribution in the heated and unheated portions of the sample are given in the figure with the full chemical analysis provided in Appendix B.

heating pulses. This enabled, in some cases, to observe the successive phase appearing of SiO_2 and FeSi-fcc phase. The detection of SiO_2 peaks at low diffraction angles remains difficult. This is partly due to technical aspects such as the limited coverage of the AGIPD, which only collects partial diffraction rings window. Further experiments are necessary to confirm the repeatability and validate this technique as a way to circumvent a long-reported inherent issue to the LH-DAC method.

Success would open up a new pathway for future "chemical-migration limited" experiment" giving access to

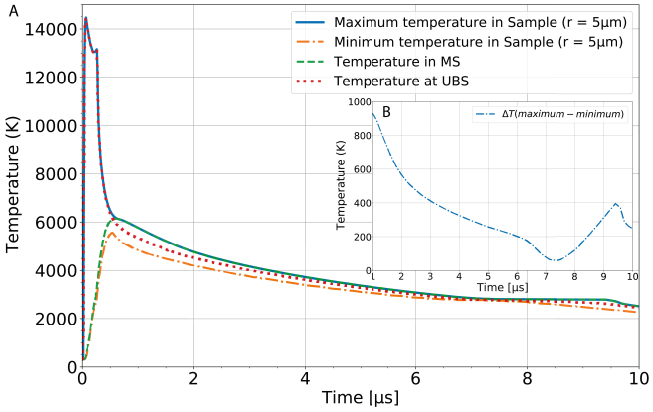

FIG. 9. A. FEM model temperatures (K) as a function of time (µs) at different points of the geometry. The red dotted line represents the temperature at the upper border of the sample (UBS) whereas the green dashed line stands for the temperature in the middle of the sample (MS), both lying on the axis of symmetry. The two other temperature curves show minimum (orange dotted-dashed line) and maximum (blue continuous line) temperatures inside of the X-ray sampled zone (cylinder of 5 µm radius). B. Difference between the minimum and maximum temperature reached inside the X-ray sampled zone. It can be observed that a local temperature gradient minimum is reached around 7.25 µs where the maximum temperature difference inside the X-ray sampled zone is only 70 K

phase diagrams and melting curves of by now never explored phases and alloys. In that frame COMSOL simulations are required to solve for temperature gradients, particularly strong during the first microseconds of the heating phase, as well as to provide accurate global temperature evolution and constrain the amount of thermal pressure. Model and experimental data are complementary for X-ray diffraction data interpretation. Models can constrain the contribution of the different phenomena leading to the chemical migration, knowledge which in turn could lead to adapted experimental designs. For higher accuracy in experiment reproduction, future models should include deformations, take into account reported non-isotropy[45], liquid-liquid interface movements (PTM/sample) as well as phase separation and grain growth.

VI. SUPPLEMENTARY MATERIAL

Data recorded for the experiment at the European XFEL are available at doi:10.22003/XFEL.EU-DATA-XXXXXX-XX."

ACKNOWLEDGMENTS

The authors are indebted to the HIBEF user consortium for the provision of instrumentation and staff that enabled this experiment. We acknowledge European XFEL in Schenefeld, Germany, for provision of X-ray free-electron laser beamtime at Scientific Instrument HED (High Energy Density Science) and would like to thank the staff for their assistance. Thanks for the sleepless nights spent for the experiments

without which we wouldn't have all that nice results. This research was supported through the European Union's Horizon 2020 research and innovation program (ERC grant 864877) as well as UKRI STFC grant ST/V000527/1. Thank you to James Moore for the help with the FIB. KB would like to acknowledge funding by Deutsche Forschungsgemeinschaft via Ap 262/2-2 within the DFG-FOR2440 HP4.

[1]L. T. Elkins-Tanton, "Magma oceans in the inner solar system," Annual Review of Earth and Planetary Sciences **40**, 113–139 (2012).

[2]L. Schaefer and L. T. Elkins-Tanton, "Magma oceans as a critical stage in the tectonic development of rocky planets," Philosophical Transactions of the Royal Society A: Mathematical, Physical and Engineering Sciences **376**, 20180109 (2018), https://royalsocietypublishing.org/doi/pdf/10.1098/rsta.2018.0109.

[3]G. Morard, S. Boccato, A. D. Rosa, S. Anzellini, F. Miozzi, L. Henry, G. Garbarino, M. Mezouar, M. Harmand, F. Guyot, E. Boulard, I. Kantor, T. Irifune, and R. Torchio, "Solving controversies on the iron phase diagram under high pressure," Geophysical Research Letters **45**, 11,074–11,082 (2018), https://agupubs.onlinelibrary.wiley.com/doi/pdf/10.1029/2018GL079950.

[4]S. Anzellini, A. Dewaele, M. Mezouar, P. Loubeyre, and G. Morard, "Melting of iron at earth's inner core boundary based on fast x-ray diffraction," Science (New York, N.Y.) **340**, 464–6 (2013).

[5]R. Sinmyo, K. Hirose, and Y. Ohishi, "Melting curve of iron to 290 gpa determined in a resistance-heated diamond-anvil cell," Earth and Planetary Science Letters **510**, 45–52 (2019).

[6]V. Prakapenka, G. Shen, and L. Dubrovinsky, "Carbon transport in diamond anvil cell," High Temperatures-high Pressures - HIGH TEMP-HIGH PRESS **35-6**, 237–249 (2010).

[7]O. T. Lord and W. Wang, "Mirrors: A matlab® gui for temperature measurement by multispectral imaging radiometry," Review of Scientific Instruments **89**, 104903 (2018), https://doi.org/10.1063/1.5041360.

[8]A. Kavner and W. Panero, "Temperature gradients and evaluation of thermoelastic properties in the synchrotron-based laser-heated diamond cell," Physics of the Earth and Planetary Interiors **143-144**, 527–539 (2004).

[9]Z. Du, G. Amulele, L. Robin Benedetti, and K. K. M. Lee, "Mapping temperatures and temperature gradients during flash heating in a diamond-anvil cell," Review of Scientific Instruments **84**, 075111 (2013), https://doi.org/10.1063/1.4813704.

[10]C. E. Lesher and D. Walker, "Cumulate maturation and melt migration in a temperature gradient," jgr **93**, 10,295–10,311 (1988).

[11]R. Sinmyo and K. Hirose, "The soret diffusion in laser-heated diamond-anvil cell," Physics of the Earth and Planetary Interiors **180**, 172–178 (2010).

[12]K. Hirose, G. Morard, R. Sinmyo, K. Umemoto, J. Hernlund, G. Helffrich, and S. Labrosse, "Crystallization of silicon dioxide and compositional evolution of the earth's core." Nature **543**, 99–102 (2017).

[13]R. Sinmyo, K. Hirose, D. Nishio-Hamane, Y. Seto, K. Fujino, N. Sata, and Y. Ohishi, "Partitioning of iron between perovskite/postperovskite and ferropericlase in the lower mantle," Journal of Geophysical Research: Solid Earth **113** (2008), https://doi.org/10.1029/2008JB005730, https://agupubs.onlinelibrary.wiley.com/doi/pdf/10.1029/2008JB005730.

[14]M. A. Baron, G. Fiquet, G. Morard, F. Miozzi, I. Esteve, B. Doisneau, A. S. Pakhomova, Y. Ricard, and F. Guyot, "Melting of basaltic lithologies in the earth's lower mantle," Physics of the Earth and Planetary Interiors , 106938 (2022).

[15]D. J. Stevenson, "On the role of surface tension in the migration of melts and fluids," Geophysical Research Letters **13**, 1149–1152 (1986), https://agupubs.onlinelibrary.wiley.com/doi/pdf/10.1029/GL013i011p01149.

[16]N. Gomez-Perez, J. F. Rodriguez, and R. S. McWilliams, "Finite element modeling of melting and fluid flow in the laser-heated diamond-anvil cell," Journal of Applied Physics **121**, 145904 (2017), https://doi.org/10.1063/1.4979313.

[17]H. P. Liermann, Z. Konôpková, K. Appel, C. Prescher, A. Schropp, V. Cerantola, R. J. Husband, J. D. McHardy, M. I. McMahon, R. S. McWilliams, C. M. Pépin, J. Mainberger, M. Roeper, A. Berghäuser, H. Damker, P. Talkovski, M. Foese, N. Kujala, O. B. Ball, M. A. Baron, R. Briggs, M. Bykov, E. Bykova, J. Chantel, A. L. Coleman, H. Cynn, D. Dattelbaum, L. E. Dresselhaus-Marais, J. H. Eggert, L. Ehm, W. J. Evans, G. Fiquet, M. Frost, K. Glazyrin, A. F. Goncharov, H. Hwang, Z. Jenei, J.-Y. Kim, F. Langenhorst, Y. Lee, M. Makita, H. Marquardt, E. E. McBride, S. Merkel, G. Morard, E. F. O'Bannon, III, C. Otzen, E. J. Pace, A. Pelka, J. S. Pigott, V. B. Prakapenka, R. Redmer, C. Sanchez-Valle, M. Schoelmerich, S. Speziale, G. Spiekermann, B. T. Sturtevant, S. Toleikis, N. Velisavljevic, M. Wilke, C.-S. Yoo, C. Baehtz, U. Zastrau, and C. Strohm, "Novel experimental setup for megahertz x-ray diffraction in a diamond anvil cell at the high energy density (hed) instrument of the european x-ray free-electron laser (euxfel)." J Synchrotron Radiat. **28 Pt 3**, 688–706 (2021).

[18]A. J. Campbell, L. Danielson, K. Righter, C. T. Seagle, Y. Wang, and V. B. Prakapenka, "High pressure effects on the iron–iron oxide and nickel–nickel oxide oxygen fugacity buffers," Earth and Planetary Science Letters **286**, 556–564 (2009).

[19]F. Farah, K. K. M. Lee, and M. C. Akin, "Temperature distribution in a laser-heated diamond anvil cell as described by finite element analysis," AIP Advances **12**, 105218 (2022), https://doi.org/10.1063/5.0094377.

[20]J.-P. Poirier, "Light elements in the earth's outer core: A critical review," Physics of the Earth and Planetary Interiors **85**, 319–337 (1994).

[21]U. Zastrau, K. Appel, C. Baehtz, O. Baehr, L. Batchelor, A. Berghäuser, M. Banjafar, E. Brambrink, V. Cerantola, T. E. Cowan, H. Damker, S. Dietrich, S. Di Dio Cafiso, J. Dreyer, H.-O. Engel, T. Feldmann, S. Findeisen, M. Foese, D. Fulla-Marsa, S. Göde, M. Hassan, J. Hauser, T. Herrmannsdörfer, H. Höppner, J. Kaa, P. Kaever, K. Knöfel, Z. Konôpková, A. Laso García, H.-P. Liermann, J. Mainberger, M. Makita, E.-C. Martens, E. E. McBride, D. Möller, M. Nakatsutsumi, A. Pelka, C. Plueckthun, C. Prescher, T. R. Preston, M. Röper, A. Schmidt, W. Seidel, J.-P. Schwinkendorf, M. O. Schoelmerich, U. Schramm, A. Schropp, C. Strohm, K. Sukharnikov, P. Talkovski, I. Thorpe, M. Toncian, T. Toncian, L. Wollenweber, S. Yamamoto, and T. Tschentscher, "The High Energy Density Scientific Instrument at the European XFEL," Journal of Synchrotron Radiation **28**, 1393–1416 (2021).

[22]H.-P. Liermann, Z. Konôpková, K. Appel, H.-G. Damker, A. Schropp, R. S. Mcwilliams, A. Goncharov, and C. Beahtz, "Conceptual design report for diamond anvil cell setup (dac) at the hed instrument of the european xfel," Journal of Synchrotron Radiation **28** (2016), https://doi.org/10.1107/S1600577521002551.

[23]Y. Fei and Y. Wang, "High-pressure and high-temperature powder diffraction," Reviews in Mineralogy and Geochemistry **41**, 521–557 (2000).

[24]R. Boehler and K. D. Hantsetters, "New anvil designs in diamond-cells," High Pressure Research **24**, 391 – 396 (2004).

[25]C. Prescher and V. B. Prakapenka, "Dioptas: a program for reduction of two-dimensional x-ray diffraction data and data exploration," High Pressure Research **35**, 223–230 (2015), https://doi.org/10.1080/08957959.2015.1059835.

[26]S. Tateno, T. Komabayashi, and K. Hirose, "Static compression of b2 kcl to 230 gpa and its p-v-t equation of state," American Mineralogist **104** (2019), 10.2138/am-2019-6779.

[27]A. Dewaele, A. Belonoshko, G. Garbarino, F. Occelli, P. Bouvier, M. Hanfland, and M. Mezouar, "High-pressure–high-temperature equation of state of kcl and kbr," Phys. Rev. B **85** (2012), 10.1103/PhysRevB.85.214105.

[28]J. Meza-Galvez, N. Gomez Perez, A. Marshall, A. Coleman, K. Appel, H.-P. Liermann, M. Mcmahon, Z. Konôpková, and R. McWilliams, "Thermomechanical response of thickly tamped targets and diamond anvil cells under pulsed hard x-ray irradiation," Journal of Applied Physics **127**, 195902 (2020).

[29]H. Hwang, T. Kim, H. Cynn, T. Vogt, R. J. Husband, K. Appel, C. Baehtz, O. B. Ball, M. A. Baron, R. Briggs, M. Bykov, E. Bykova, V. Cerantola, J. Chantel, A. L. Coleman, D. Dattlebaum, L. E. Dresselhaus-Marais, J. H. Eggert, L. Ehm, W. J. Evans, G. Fiquet, M. Frost, K. Glazyrin, A. F. Goncharov, Z. Jenei, J. Kim, Z. Konôpková, J. Mainberger, M. Makita, H. Marquardt, E. E. McBride, J. D. McHardy, S. Merkel, G. Morard, E. F. I. O'Bannon, C. Otzen, E. J. Pace, A. Pelka, C. M. Pépin, J. S. Pigott, V. B. Prakapenka, C. Prescher, R. Redmer, S. Speziale, G. Spiekermann, C. Strohm, B. T. Sturtevant, N. Velisavljevic, M. Wilke, C.-S. Yoo, U. Zastrau, H.-P. Liermann, M. I. McMahon, R. S. McWilliams, and Y. Lee, "X-ray free electron laser-induced synthesis of ϵ-iron nitride at high pressures," The Journal of Physical Chemistry Letters **12**, 3246–3252 (2021), pMID: 33764078, https://doi.org/10.1021/acs.jpclett.1c00150.

[30]D. Greiffenberg, "The agipd detector for the european xfel," Journal of Instrumentation **7** (2012).

[31]A. Allahgholi, J. Becker, A. Delfs, R. Dinapoli, P. Goettlicher, D. Greiffenberg, B. Henrich, H. Hirsemann, M. Kuhn, R. Klanner, A. Klyuev, H. Krueger, S. Lange, T. Laurus, A. Marras, D. Mezza, A. Mozzanica, M. Niemann, J. Poehlsen, J. Schwandt, I. Sheviakov, X. Shi, S. Smoljanin, L. Steffen, J. Sztuk-Dambietz, U. Trunk, Q. Xia, M. Zeribi, J. Zhang, M. Zimmer, B. Schmitt, and H. Graafsma, "The Adaptive Gain Integrating Pixel Detector at the European XFEL," Journal of Synchrotron Radiation **26**, 74–82 (2019).

[32]P. Saha and G. D. Mukherjee, "Thermal conductivity of iron and nickel during melting: Implication to planetary liquid outer core," (2021), arXiv:2105.08962 [cond-mat.mtrl-sci].

[33]A. Dewaele, G. Fiquet, and P. Gillet, "Temperature and pressure distribution in the laser-heated diamond–anvil cell," Review of Scientific Instruments **69**, 2421–2426 (1998), https://doi.org/10.1063/1.1148970.

[34]C. E. Yen, Q. Williams, and M. Kunz, "Thermal pressure in the laser-heated diamond anvil cell: A quantitative study and implications for the density versus mineralogy correlation of the mantle," Journal of Geophysical Research: Solid Earth **125**, e2020JB020006 (2020), e2020JB020006 2020JB020006, https://agupubs.onlinelibrary.wiley.com/doi/pdf/10.1029/2020JB020006.

[35]F. Miozzi, J. Matas, N. Guignot, J. Badro, J. Siebert, and G. Fiquet, "A new reference for the thermal equation of state of iron," Minerals **10** (2020), 10.3390/min10020100.

[36]N. Tsujino, Y. Nishihara, Y. Nakajima, E. Takahashi, K.-i. Funakoshi, and Y. Higo, "Equation of state of γ-fe: Reference density for planetary cores," Earth and Planetary Science Letters **375**, 244–253 (2013).

[37]Y. Kuwayama, G. Morard, Y. Nakajima, K. Hirose, A. Q. R. Baron, S. I. Kawaguchi, T. Tsuchiya, D. Ishikawa, N. Hirao, and Y. Ohishi, "Equation of state of liquid iron under extreme conditions," Phys. Rev. Lett. **124**, 165701 (2020).

[38]G. Morard, G. Garbarino, D. Antonangeli, D. Andrault, N. Guignot, J. Siebert, M. Roberge, E. Boulard, A. Lincot, A. Denoeud, and S. Petitgirard, "Density measurements and structural properties of liquid and amorphous metals under high pressure studied by in situ x-ray scattering"." High Pressure Research **34** (2013), 10.1080/08957959.2013.860137.

[39]M. Hass, J. A. Harrington, D. A. Gregory, and J. W. Davisson, "Infrared absorption limits of hf and df laser windows," Applied Physics Letters **28**, 610–611 (1976), https://doi.org/10.1063/1.88584.

[40]S. Webster, Y. Chen, G. Turri, A. Bennett, B. Wickham, and M. Bass, "Intrinsic and extrinsic absorption of chemical vapor deposition single-crystal diamond from the middle ultraviolet to the far infrared," J. Opt. Soc. Am. B **32**, 479–484 (2015).

[41]A. Savvatimskiy and S. Onufriev, "Specific heat of liquid iron from the melting point to the boiling point," High Temperature **56**, 933–935 (2018).

[42]Z. Konôpková, R. McWilliams, N. Gomez-Perez, and A. Goncharov, "Direct measurement of thermal conductivity in solid iron at planetary core conditions," Nature **534**, 99–101 (2016).

[43]C. D. Chliatzou, M. J. Assael, K. D. Antoniadis, M. L. Huber, and W. A. Wakeham, "Reference correlations for the thermal conductivity of 13 inorganic molten salts," Journal of Physical and Chemical Reference Data **47**, 033104 (2018), https://doi.org/10.1063/1.5052343.

[44]A. Kirshenbaum, J. Cahill, P. McGonigal, and A. Grosse, "The density of liquid nacl and kcl and an estimate of their critical constants together with those of the other alkali halides," Journal of Inorganic and Nuclear Chemistry **24**, 1287–1296 (1962).

[45]S. S. Lobanov and Z. M. Geballe, "Non-isotropic contraction and expansion of samples in diamond anvil cells: Implications for thermal conductivity at the core-mantle boundary," Geophysical Research Letters **49**, e2022GL100379 (2022), e2022GL100379 2022GL100379, https://agupubs.onlinelibrary.wiley.com/doi/pdf/10.1029/2022GL100379.

[46]E. Edmund, M. Morard, G.and Baron, A. Rivoldini, S. Yokoo, S. Boccato, K. Hirose, and A. P. . D. Antonangeli., "The fe-fesi phase diagram at mercury's core conditions." Nature communications **13** (2022), https://doi.org/10.1038/s41467-022-27991-9.

[47]E. Edmund, D. Antonangeli, F. Decremps, G. Morard, S. Ayrinhac, M. Gauthier, E. Boulard, M. Mezouar, M. Hanfland, and N. Guignot, "Structure and elasticity of cubic fe-si alloys at high pressures," Phys. Rev. B **100**, 134105 (2019).

[48]R. A. Fischer, A. J. Campbell, D. M. Reaman, N. A. Miller, D. L. Heinz, P. Dera, and V. B. Prakapenka, "Phase relations in the fe–fesi system at high pressures and temperatures," Earth and Planetary Science Letters **373**, 54–64 (2013).

[49]D. Andrault, L. Pison, G. Morard, G. Garbarino, M. Mezouar, M. A. Bouhifd, and T. Kawamoto, "Comment on: Melting behavior of SiO_2 up to 120 GPa (Andrault et al. 2020)," Physics and Chemistry of Minerals **49**, 3 (2022).

[50]Y. Mori, H. Tateno, K. Hirose, R. Sinmyo, S. Tateno, G. Morard, and Y. Ohishi, "Melting experiments on fe–fe3s system to 254 gpa," Earth and Planetary Science Letters **464**, 135–141 (2017).

[51]G. Morard, D. Andrault, D. Antonangeli, Y. Nakajima, A. Auzende, E. Boulard, S. Cervera, A. Clark, O. Lord, J. Siebert, V. Svitlyk, G. Garbarino, and M. Mezouar, "Fe–feo and fe–fe 3 c melting relations at earth's core–mantle boundary conditions: Implications for a volatile-rich or oxygen-rich core," Earth and Planetary Science Letters **473**, 94–103 (2017).

[52]J. Li, Q. Wu, J. Li, T. Xue, Y. Tan, X. Zhou, Y. Zhang, Z. Xiong, Z. Gao, and T. Sekine, "Shock melting curve of iron: A consensus on the temperature at the earth's inner core boundary," Geophysical Research Letters **47** (2020), 10.1029/2020GL087758.

[53]D. Zhou, J. Dong, Y. Si, F. Zhu, and J. Li, "Melting curve of potassium chloride from in situ ionic conduction measurements," Minerals **10** (2020), 10.3390/min10030250.

[54]T. Komabayashi, "Thermodynamics of melting relations in the system fe-feo at high pressure: Implications for oxygen in the earth's core," Journal of Geophysical Research: Solid Earth **119**, 4164–4177 (2014), https://agupubs.onlinelibrary.wiley.com/doi/pdf/10.1002/2014JB010980.

[55]J.-P. Poirier, *Earth's Interior - second edition* (Cambridge University Press, 2008).

[56]A. C. Hindmarsh, P. N. Brown, K. E. Grant, S. L. Lee, R. Serban, D. E. Shumaker, and C. S. Woodward, "Sundials: Suite of nonlinear and differential/algebraic equation solvers," ACM Transactions on Mathematical Software (TOMS) **31**, 363–396 (2005).

[57]O. Schenk and K. Gärtner, "Solving unsymmetric sparse systems of linear equations with pardiso," Future Generation Computer Systems **20**, 475–487 (2004).

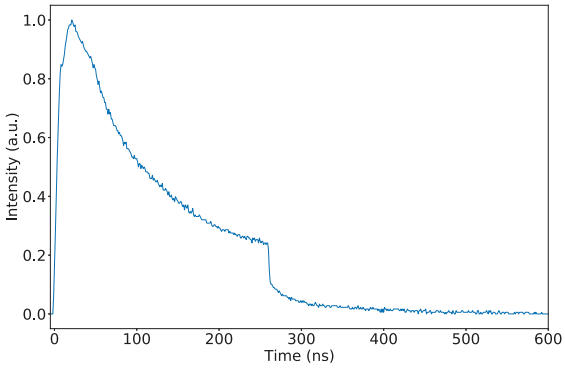

FIG. 10. Time evolution of the fiber laser intensity I_{meas}, acquired with an oscilloscope at the EuXFEL, and used in our experiments. The intensity has been normalized here to have a unit maximum intensity.

Appendix A: Laser and X-ray beams temporal evolution

To ensure a high model fidelity with the real experimental conditions, the time dependency of the fiber laser intensity was included. This intensity variation was measured by an oscilloscope and is plotted in figure 10 with a 994 values file directly implemented in the model.

The X-ray pulse train series used in the model was implemented by reproducing a series of gaussian pulses 11. The temporal width of each pulse (P_{dur}) is the same, linked to the standard deviation σ_t=100 fs by $P_{dur} = \sigma_t \times [2\sqrt{2\ln 2}]$. In the following a pulse is a truncated Gaussian curve within a range of $[-4 \times \sigma_t, 4 \times \sigma_t]$. Duration between pulses is kept constant and is related to the frequency by $P_X = 1/f_X$, with $f_X = 2.27$ MHz such that an X-ray pulse hits the sample every 440 ns. Finally, we decided not to start the first pulse of the series at exactly zero due to numerical issues when dealing with extremely small numbers (of the order of the machine precision). Therefore, the first pulse is chosen to start at $128 \times \sigma_t$ which corresponds to a reasonably "numerically detectable" starting duration for the COMSOL software. We generated value files including 50 values per pulse, each pulse in the around the maximum peak value and zeros elsewhere. This file is then imported into our COMSOL model. It is hereby important to notify that the software reduces the precision.

To reproduce the incoming energy due to the X-ray pulse train, we generate a series of Gaussian pulses (40 in that specific case) at a frequency of 2.27 MHz. Each pulse is assumed to have the exact same duration with the standard deviation given by $\sigma_t = S_{Diam}/[2\sqrt{2\ln 2}]$). Pulse peak intensity is known to vary within a pulse train and was therefore normalized to 1 as the maximum of the highest intensity. In order to ensure a realistic agreement between the model and experimental results, we impacted the X-ray intensity variations measured during our runs onto this bunch of pulses (Supp. Mat.). Each pulse of the train was weighted by the measured

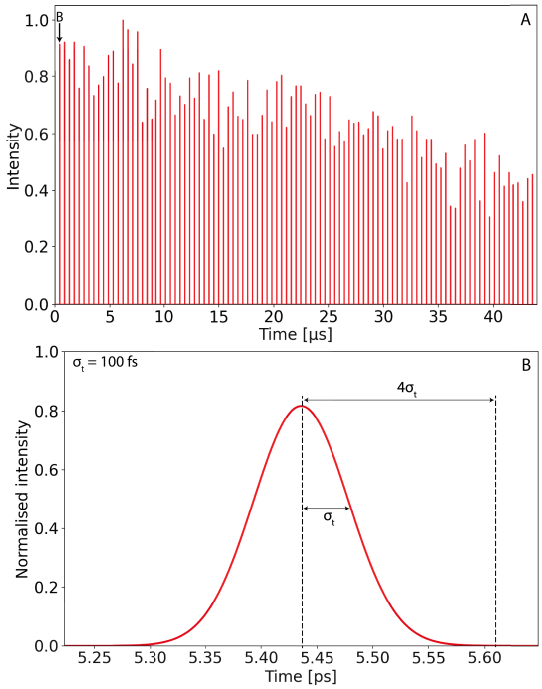

FIG. 11. A. Pulse series example for a run showing intensity variation inside a pulse train (in a.u.) as a function of time (in µs). B. Focus on single X-ray pulse intensity as a function of time. Intensity is normalized to 1 which corresponds to the maximum intensity reached in the pulsed train.

intensity. Details about the exact pulse series generation procedure used for the model are given in figure 11. Fig. 11 A plots the entire pulse train normalized to 1 as the maximum intensity reached in the entire train. Fig. 11 B highlights the shape of the first pulse.

Appendix B: FIB cutting chemical analysis

An FEI HELIOS G4 UC FIB/SEM was used to access the heating spots and check for apparent chemical migration phenomena. The shot observation combined with chemical analysis with an EDS detector demonstrated that no apparent chemical migration occurred for short laser heating. In addition, supplementary *post mortem* analysis was achieved by doing a FIB cutting. Along FIB cutting, chemical analysis was performed with a Helios G4 UC FIB/SEM. Table III lists the measured concentrations in each element in weight percent (wt%) and figure 12 refers to the localization of each measurement (8 in total). Depletion of up to 3.15 wt% of O and 3.56 wt% of Si and enrichment up to 6.17 wt% iron were observed in the heating spot compared to the pristine sample. However this is the highest observed difference and certain spot show differences as low as 0.73 wt% of O (pt2 vs pt8), 0.39 wt% of Si (pt2 vs pt 6) and 0.59 wt% Fe (pt2 vs pt5). We estimate the error bar on the chemical measurements to

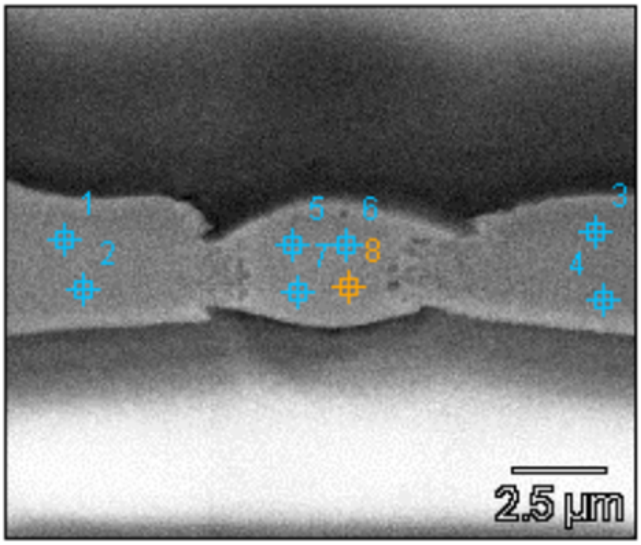

FIG. 12. Localization of chemical EDS analysis. Points refer to Table III

Meas. point/ chem. species	O	Si	Cl	K	Fe
Point 1	5.63	10.61	1.02	1.11	81.63
Point 2	5.04	9.4	0.93	1.07	83.57
Point 3	6.23	11.53	0.99	1.05	80.2
Point 4	5.53	10.11	1.02	0.94	82.4
Point 5	4.21	8.98	1.47	1.18	84.16
Point 6	3.71	9.01	1.7	1.17	84.41
Point 7	3.08	7.97	1.54	1.05	86.37
Point 8	4.31	8.76	1.32	1.07	84.54

TABLE III. Concentration measurements from FIB (in wt%)

be relatively larger than conventional microprobe measurements, as we were only able to perform EDS measurements in a tilted geometry during FIB cut. However, the present measurements are used to characterize the chemical migration, i.e. the relative composition between unheated starting material and center of the laser heated hotspot.

Appendix C: Details on our numerical model

Modeling the DAC geometry with a simple Cartesian 2D model is possible, but it would discard our DAC symmetry of revolution. With nearly the same numerical cost, our DAC is better modeled by an axisymmetric model[28], assuming only radial or axial variations and using a 2D mesh (figure 4). Such a model represents accurately the real DAC provided that the laser-heating is well centered on the axis of symmetry, and discarding possible three-dimensional effects (which could e.g. be due to liquid flows[16]).

1. Pressure induced thickness variation

Regarding the thicknesses mentioned in Table I, the second value corresponds to the theoretical thickness obtained after compression. That thickness variation of the sample with pressure in DAC experiments depends on the material and therefore is related to the EoS (ϵ-Iron[35], liquid iron[37], B2-KCl[27]).

In order to have directly an expression for the volume we solve the EoS to obtain a multivariate polynomial under the $V(P,T)$ form which is then used for thickness calculations. We calculated the volume of the sample V_S considering the case of a perfect cylinder

$$V_S = \pi R_3^2 \delta_3 \tag{C1}$$

where R_3 is the sample radius, and δ_3 the sample thickness before compression. We consider the simplified case where deformations in the radial direction are neglectable upon first compression due to the gasket resistance. Thus, the sample is only considered to deform in the axial direction (meaning in its thickness). From there on we calculate the initial number of lattice elements N_e in the DAC at ambient pressure

$$N_e = V/V_0, \tag{C2}$$

where V_0 is the sample volume at ambient pressure and temperature which can be found using material properties available in the literature. We assume that the number of lattices remains constant in the sample during compression. The lattice volume is then calculated at the experimental pressure of the DAC using the multivariate polynomial providing $V(P_{ref})$. Finally, we calculate the thickness by rewriting (C1) and including the initial number of lattice elements and their new volume at the desired pressure

$$\delta_3(P_{ref}) = \frac{N_e V(P_{ref})}{\pi R_3^2} \tag{C3}$$

with R_3 being the sample radius. The thickness of the sample as well as that of the PTM are calculated this way as a function of the initial pressure in the DAC. The thickness is then considered being constant during the simulation as no expansion is allowed over the sample.

2. Thermal heating due to radiation absorption

In the DAC, the temperature rise is generated by the material absorption of the laser and X-ray beams emitted along the z-axis. In the following, we first consider the intensity of a single beam, incident on the diamond surface; the total intensity in our numerical model is then simply the linear superposition of the laser and X-ray radiation beam intensities.

In each material, the absorption of this single radiation beam is assumed to be governed by the Beer-Lambert law[28], and the absorption occurs on a typical length scale that depends on the radiation frequency and on the material. When this length scale is very small compared to the material layer

thickness, i.e. for opaque material, this volume absorption can be approximated by a boundary heat source, avoiding the fine mesh that would be required otherwise (see details in section C 3). In such opaque materials, the radiation intensity is zero below the material surface, and the volume heat source due to radiation absorption is discarded ($Q = 0$). In the opposite case, the volume absorption in the semi-transparent material layer (k) has to be considered. Considering the radiation intensity I due to the single beam along the unit vector $\hat{\boldsymbol{I}}$, the Beer-Lambert law reads

$$\nabla I = -\mu_k \, I \, \hat{\boldsymbol{I}}, \tag{C4}$$

which integrates into (along $\hat{\boldsymbol{I}}$, i.e. along the z-axis here)

$$I = I_k^{in} \mathrm{e}^{-\mu_k H_k} \tag{C5}$$

for a constant (Napierian) attenuation coefficient μ_k, which depends naturally on the radiation beam frequency content. Here, $H_k = \pm(z - z_k)$ is the penetration depth in the material (k), the sign depending on the radiation direction and z_k being the z-position of the surface layer that the radiation is incident on. In this material (k), the volume heat source Q_k is then simply given by $Q_k = \mu_k I$.

In principle, μ_k also depends on temperature and pressure, and thus on space, which requires the integration of the partial differential equation (C4). These dependencies being however not well known in our case, constant values have been used for μ_k in our model (Table II). The numerical cost associated with the integration of equation (C4) has then been avoided by using directly the analytical solution (C5) in the model. Table IV provides the various analytical expressions used in the model to reproduce the incoming laser and X-ray intensities and their interaction with the material through absorption (required to calculate Q_k).

Since the total intensity I_k^{tot} incident on the material layer (k) boundary can be partially reflected, the actual incoming intensity I_k^{in} in equation (C5) is $I_k^{in} = (1 - \mathcal{R}_k) I_k^{tot}$, with the material reflection coefficient $\mathcal{R}_k$. Since $\mathcal{R}_k$ is insufficiently known and depends on many parameters like the radiation frequency, the surface roughness or the temperature, all the reflection coefficients are set to $\mathcal{R}_k = 0$ in our model.

Before entering any material or any reflection, the total intensity I_0^{tot} of the radiation incident on the diamond is modeled with a Gaussian spatial distribution such that

$$I_0^{tot} = I_m \, I_t(t) \, \exp\left(-\frac{r^2}{2\sigma_r^2}\right), \tag{C6}$$

where $\sigma_r = S_{Diam}/[2\sqrt{2\ln 2}]$ is a Gaussian radius parameter related to the radiation FWHM spot diameter S_{Diam}, and with r the cylindrical radius coordinate (distance from the model symmetry axis). Since the absolute value of the maximum intensity I_m is generally not known for the experiments (both for the laser and the X-ray beam), it is here a model adjustable parameter that is fixed to obtain a good agreement between the experimental and the numerical results. By contrast, the temporal evolution $I_t(t)$ imposed in the model is obtained from measurements or modelling of the pulses (see also Appendix A). Integrating equation (C6) in space and time provides the pulse energy E_p as[28]

$$E_p = 2\pi\sigma_r^2 I_m \mathcal{E} \tag{C7}$$

where $\mathcal{E} = \int_t I_t(t)\mathrm{d}t$.

3. Boundary conditions and initial state

To integrate equations (1)-(2), boundary conditions are needed at the external diamond and gasket boundaries.

Heat loss through convection and radiation should usually be considered but as the DAC is placed in vacuum, only radiation plays a role. Yet regarding the possible need of including both ways of heat transfer for future models, more details upon heat transfer are given in supplementary material. For the temperature T, two conditions have been used here. Either a constant external temperature T_{ext} has been imposed at the external boundaries, or heat loss through radiation is considered following in our case a $q_s = \sigma_s(T^4 - T_{ext}^4)$ law with the Stefan-Boltzmann constant $\sigma_s = 5.67 \cdot 10^{-8}$ W.m^{-2}.K^{-4}. Here $T_{ext} = 300$ K is used, and both conditions lead actually to the same results. Indeed, external boundaries are very far from the maximum thermal heating, and the effect of the boundary condition choice can thus be expected to be negligible.

Boundary conditions are also required for the elastic part, and the zero displacement constraint $\boldsymbol{u} = \boldsymbol{0}$ has been imposed at all external boundaries. Note that the thermal pressure P_{th} would naturally be zero if all external boundaries can move freely, and displacement constraints are thus required, at least at certain boundaries, to generate a thermal pressure (preliminary tests have been performed by setting $\boldsymbol{u} = \boldsymbol{0}$ for the diamonds or the gasket only).

In opaque materials, like the metallic sample considered in our experiments, the attenuation coefficient μ is very large and the radiation induced thermal heating occurs then on the very small typical length scale μ^{-1}. This would require a very fine mesh to reproduce the intensity variations given by the Beer-Lambert (volume) absorption equation (C5). To avoid the associated numerical cost, one can rather replace this volume absorption by a boundary heat source, assuming that all the (non-reflected) radiation energy flux I_k^{in} is converted into heat at the material surface (which is equivalent to assume an infinite absorption coefficient for the material). At these boundaries, the normal heat flux is thus imposed to be I_k^{in}. This approach has been benchmarked by checking that the results obtained this way are the same than those obtained with a Beer-Lambert volume absorption model (integrated on a fine mesh). In the simulations shown in this work, such a boundary heat source has only been used at the sample surface, the least being highly absorbing (i.e. opaque) at laser wavelength. Note that this boundary heat source approach reduces the numerical cost while keeping realistic physical behaviour. Rather thin meshes are yet required and a numerical convergence study has to be carefully performed to ensure the numerical accuracy of the results.

Medium	X-ray volume heat source	laser volume heat source
Upstream Diam[a]	$I^{tot}_{X_0}\mu_{X_1}\exp(\mu_{X_1}(z-(\delta_1{}^{\text{b}}+\delta_2{}^{\text{c}}+0.5\delta_3{}^{\text{d}})))$	$I^{tot}_{L_0}\alpha_1\exp(\mu_{L_1}(z-(\delta_1+\delta_2+0.5\delta_3)))$
Upstream PTM	$I^{tot}_{X_1}\mu_{X_2}\exp(\mu_{X_2}(z-(\delta_2+0.5\delta_3)))\exp(-\mu_{X_1}\delta_1)$	$I^{tot}_{L_1}\mu_{L_2}\exp(\mu_{L_2}(z-(\delta_2+0.5\delta_3)))\exp(-\mu_{L_1}\delta_1)$
Sample	$I^{tot}_{X_2}\mu_{X_3}\mathrm{e}^{-\mu_{X_2}(z+\delta_2+0.5\delta_3)}\exp(-\mu_{X_1}\delta_1)\exp(-\mu_{X_2}\delta_2)$	$\varnothing$
Downstream PTM	$I^{tot}_{X_3}\mu_{X_2}\exp(-\mu_{X_2}(z+\delta_2+0.5\delta_3))\varpi$	$I^{tot}_{L_1}\mu_{L_2}\exp(\mu_{L_2}(z-(\delta_2+0.5\delta_3)))\exp(-\mu_{L_1}\delta_1)$
Downstream Diam	$I^{tot}_{X_4}\mu_{X_1}\exp(-\mu_{X_1}(z+(\delta_1+\delta_2+0.5\delta_3)))\exp(-\mu_{X_4}\delta_4)\varpi$	$I^{tot}_{L_0}\mu_{L_1}\exp(\mu_{L_1}(z-(\delta_1+\delta_2+0.5\delta_3)))$

[a] Diamond
[b] Diamond thickness
[c] PTM thickness
[d] Sample thickness

TABLE IV. List of the Beer-Lambert derived analytical solutions for $Q_k = \mu_k I$, as used in COMSOL, noting $\varpi = \exp(-\mu_{X_1}\delta_1)\exp(-\mu_{X_2}\delta_2)\exp(-\mu_{X_3}\delta_3)$. Absorption coefficients were adapted depending on the heating source wavelength (X-ray or laser). Formula for the sample only applies in the case of X-rays, wavelength at which Fe is semi-transparent on the contrary to fiber laser wavelength where all energy $I^{tot}_{L_2}$ is considered to be deposited at the surface on both sides of the sample. Numbered labels in Table IV are listed from top to bottom (1: upstream diamond, 2: upper PTM, 3: sample, 4: lower PTM, 5: downstream Diamond). Note that for the laser I^{tot}_0 and I^{tot}_5 have the same value due to two sided heating. Same for I^{tot}_4 and I^{tot}_2. μ_{X_i} and μ_{L_i} stand respectively for the X-ray and laser absorption coefficients in the i^{th} medium. The same pattern is applied for the intensities $I^{tot}_{X_i}$ and $I^{tot}_{L_i}$.

Finally, the transient response of our numerical DAC, obtained by time-stepping equations (1)-(2), heavily depends on the chosen initial state. Here, the model integration starts with a constant temperature $T(t=0) = T_{ext} = 300$ K and with the zero initial displacement $\boldsymbol{u}(t=0) = \mathbf{0}$ initial state (no initial condition is required for the time derivative of $\boldsymbol{u}$, i.e. for the initial velocity, since our approach is quasi-static).

4. Heat capacity of the FCC iron

Lots of parameters rely on these EoS due to their dependency to volume, temperature and/or pressure (sample thickness, thermal conductivity, heat capacity).

In addition to material property variations with temperature and pressure along a given phase, phase variations occur upon laser, X-ray heating and compression. Those phase changes affect the material properties and were implemented by referring to the phase diagrams available in the literature. Melting curves and phase change zones were taken into account in the model by using them as conditions for parameters changes. This model uses existing melting curves for iron alloys[50,51,52] and KCl[53] (provided in supplementary material).

The specific phase change between hcp and fcc high pressure phase of iron was included in the model using a second order polynomial[3]. Phase changes are mostly related to material property modifications. Therefore we used the phase change temperature as a condition for switching EoS[35,36]. As phase changes generally go along with a release or absorption of latent heat we included as well the Apparent Heat Capacity Method (AHCM). Heat capacity variations as a function of temperature and pressure can be inferred from the formula given by Komabayashi et al. 2014[54]

$$G = G_{1bar,T} + \int_{1bar}^{P} V_T \mathrm{d}P \tag{C8}$$

where $G_{1bar,T}$ is the Gibbs free energy at $P = 1$ bar and given T expressed by

$$G_{1bar,T} = a + bT + cT\ln T + dT^2 + eT^{-1} + fT^{0.5} \tag{C9}$$

with $a = 12460.621, b = 386.99162, c = -52.2754, d = 0.000177578, e = -395355.43, f = -2476.28$ and V_T the molar volume of the corresponding phase at given T where the EoS obtained multivariate polynomial is used.

In order to obtain C_P, we use[55] :

$$S = -\left(\frac{dG}{dT}\right)_P \quad , \quad \left(\frac{dS}{dT}\right)_P = \frac{C_P}{T} \tag{C10}$$

that can be combined, leading to

$$C_P = -\left(\frac{d^2G}{d^2T}\right)_P T \tag{C11}$$

5. Phase change effects: the AHCM method

The AHCM assumes that, instead of a sharp heat capacity transition upon phase change, the transformation occurs over a temperature range ΔT, driven by a smooth transition function $\alpha(T)$. The choice of this range is important as it determines the sharpness of the transition and should ideally be wider than the biggest temperature gap from one time step to another to avoid numerical issues. This is essentially the case during the short duration where the maximum of laser intensity hits the sample. Following this idea, the material's heat capacity is then expressed as

$$C_P = C_{P_1}(1-\alpha(T)) + C_{P_2}\alpha(T) + L_{1\to 2}\frac{\partial \alpha}{\partial T} \tag{C12}$$

where C_{P_1} can be the heat capacity of a solid phase or any pure phase 1 and C_{P_2} the heat capacity of a liquid phase or any pure phase 2 and considering that for a pure phase 1: $\alpha(T) = 0$ and for a pure phase 2: $\alpha(T) = 1$ and varying continuously between both. The transition function derivative $\partial_T \alpha$ stands for the slope of this function. For the purpose

of our simulation, a temperature range of 50 K was chosen, meaning that latent heat effect will occur between half of that value below and half above the given phase change temperature. This range was chosen on purpose to be wide regarding high temperature variations occurring between some time steps of the simulation. Indeed, a narrower transition range requires a finer mesh to have precise information about the temperature differences.

Using that transition function, the thermal conductivity variations upon phase change were defined the same way but without additional latent heat term. For thermal conductivity, the transition is thus given by

$$k_{th} = \alpha(T)k_{th1} + [1 - \alpha(T)]k_{th2}. \tag{C13}$$

6. Space and time numerical discretization

We used a mesh combined of fine boundary layer type rectangular elements at the sample boundaries, and triangular mesh in the remaining domain. Both element types were set to be increasingly fine towards the sample boundaries. Diamonds and gasket are on the contrary only meshed by coarse elements regarding the low endured gradients. Using first order Lagrange elements for temperature and elastic displacement, the total number of degrees of freedom is of the 10^4 order for our numerical model.

Equations are time stepped with the built-in time-stepping scheme based on backward differentiation formula[56], and, at each time step the system is solved with the sparse direct linear solver PARDISO[57]. Note that our model involves a large disparity of time scales (down to the fs during a pulse, ns between pulses, µs for the whole simulation duration), which can lead to numerical issues. To ensure that our model takes correctly into account each X-ray pulse over the whole simulation time, the model relies on the 'events' module of COMSOL, which allow specifying the occurrence of a repeated event (forcing a small enough time step at each event).